Manuscript File

Manuscript (Unmarked):

Second-order wave run-up on a vertical circular cylinder in front of a vertical wall based on the application of quadratic transfer function in bi-directional waves

Peiwen Cong[a, c*], Bin Teng[a] and Wei Bai[b]

[a] State Key Laboratory of Coastal and Offshore Engineering, Dalian University of Technology, Dalian 116024, China

[b] Department of Computing and Mathematics, Manchester Metropolitan University, Chester Street, Manchester M1 5GD, UK

[c] Department of Civil and Environmental Engineering, National University of Singapore, 117576, Singapore

Abstract

The second-order wave run-up on a vertical circular cylinder in front of a long vertical wall was investigated. A numerical model was developed to simulate the wave diffraction caused by an arbitrarily shaped structure in the presence of bi-directional incident waves based on a higher-order boundary element method. By using the developed model, the wave elevation quadratic transfer function (QTF) in bi-directional waves, which is defined as the second-order wave run-up caused by two incident waves of unit amplitude from two directions, can be determined. The developed model was subsequently used to investigate the wave interaction with a cylinder situated near a vertical wall. The image principle was applied to transform the original problem into an equivalent one of wave diffraction caused by two symmetrical cylinders in open seas exposed to bi-directional incident waves. The second-order wave run-up on the cylinder can then be determined by using the wave elevation QTF obtained from an analysis of

the equivalent problem. A detailed numerical analysis was subsequently conducted, and the characteristics of the nonlinear wave action upon a cylinder in close proximity to a long wall were explored.

Key words:

Bi-directional waves; Image principle; QTF; Wave diffraction; Wave run-up

1. Introduction

The interaction of water waves with a structure piercing the free surface can cause the water around the structure to rise above the crest of the incoming wave. The free-surface elevation around the structure, also known as the wave run-up, can then be greatly enhanced. The wave run-up around the foundation or supporting columns of a structure is of significant importance to the suitable design of the air gap. A sufficient air gap can mitigate the wave slamming beneath the deck, and therefore avoid the potential damage caused by the wave impact.

A vertical cylinder is frequently employed as an essential component of many offshore structures, and various studies related to the wave run-up on vertical cylinders have been reported. The potential flow theory is widely applied to investigate the interaction of water waves with large-scale structures. Based on a linear wave theory, Havelock (1940) initially gave an analytical solution to the wave diffraction caused by a vertical cylinder extending from the seabed and piercing the water surface for deep-water cases. This solution was then extended to the case of a finite water depth by MacCamy and Fuchs (1954). When the cylinder is slender with respect to the wavelength, MacCamy and Fuchs (1954) assumed the scattering parameter to be small and derived an equation of the wave run-up on the weather side of the cylinder based on the asymptotic expansion of Bessel functions. To approximate the wave run-up with a better accuracy, extension of the linear wave theory to the second order was subsequently carried out by some researchers (Kim and Yue, 1989; Kriebel, 1990; Eatock Taylor and Chau, 1992; Isaacson and Cheung, 1992; Kim et al., 1997; Bai and

Teng, 2013; Shao and Faltinsen, 2013). To date, the calculation of the second-order wave run-up or wave force on a vertical cylinder or cylinder array in open seas has been conducted by some researchers, such as Chau and Eatock Taylor (1992), Malenica et al. (1999), Mavrakos and Chatjigeorgiou (2006), and Cong et al. (2015, 2018). Kim and Yue (1989) suggested that the second-order effect on the wave run-up can be significant, and the evaluation of the potentially substantial contributions that originate from the second-order effect is quite needed. By comparing the numerical predictions of the wave run-up on a large cylinder with the measured data from a laboratory experiment, Kriebel (1992) noted that the second-order wave theory generally explains a significant portion of the non-linear wave run-up measured at all angles around the cylinder. In addition, the numerical predictions based on the second-order wave theory are in much better agreement with the measured data than those based on the linear wave theory and can also agree well with the measured data for weakly non-linear incident waves. In addition to the second-order wave theory, efforts have also been made by researchers for the development of a fully non-linear theory. A fully non-linear model adopts the boundary conditions satisfied on instantaneous moving surfaces, and it can be applied to steep incident waves. The application of a fully non-linear theory in analysing the wave interaction with a cylinder or cylinder array can be found in the studies by Bai and Eatock Taylor (2007), Wang and Wu (2010), Zhou et al. (2012), and Bai et al. (2014).

To provide alternative approaches to the prediction of wave run-up, several semi-empirical equations have been proposed by researchers. Hallermeier (1976) suggested a velocity stagnation head method for the wave run-up on a vertical cylinder. This method was developed based on the assumption that the fluid particle at the wave crest is forced to convert its kinetic energy into potential energy by increasing the distance of $u^2/(2g)$ above the wave crest level, in which u is the velocity of the fluid particle at the wave crest, and g is the acceleration of gravity. Thus, the wave run-up is expressed as a summation of the wave crest elevation term and the velocity head term. This method had been applied as well to structures of other shapes, such as truncated cylinders (Niedzwecki and Duggal, 1992), cylinder arrays (Niedzwecki and Huston, 1992), cylinders seated on cone-shaped foundations (De Vos et al., 2007), and slender piles (Andersen et al., 2011; Kazeminezhad and Etemad-Shahidi, 2015; Bonakdar et al., 2016). Modifications to the equation had been made by introducing empirical coefficients that can be calibrated by fitting the measured data. Cao et al. (2017) evaluated the superiority of one empirical equation over another within a range of wave conditions and geometric parameters.

So far, extensive studies have been conducted for the wave run-up on structures in open seas. However, in recent years, various nearshore projects, such as ships and wave energy converters, have been developed. Investigation of the wave interaction with structures near a wharf or breakwater has become increasingly important, and this has attracted the attention of many researchers. Teng et al. (2004) proposed an analytical method to analyse the wave radiation caused by a moving cylinder close to a vertical wall. In their work, the wharf was approximated by a fully reflective and infinitely long vertical wall, and the image principle was used to convert the original problem into an equivalent one with two symmetrical cylinders moving in the open seas. Other researchers have adopted the image principle to investigate the wave interaction with structures in close proximity to vertical walls, such as the wave diffraction caused by a cylinder close to orthogonal walls (Ning et al., 2005), action of ship waves on a nearby cylinder situated near a wall (Sun et al., 2007), and wave diffraction due to a truncated cylinder or cylinder array in front of a wall (Zheng and Zhang, 2015; Chatjigeorgiou, 2019). Cong et al. (2019, 2020) applied the image principle to investigate the wave interaction with multiple impermeable or porous cylinders in front of a long vertical wall and derived simple relationships between the diffracted waves from real and imaginary cylinders.

Generally, the characteristic nature of a hydrodynamic problem can be better described by a non-linear analysis. However, to date, a non-linear analysis of the wave interaction with structures situated near a vertical wall has rarely been reported. Kriebel

(1992) indicated that the second-order component is an important correction to the linear wave run-up on a vertical cylinder in open seas. It can be expected that the second-order component can also contribute considerably to the wave run-up on structures near a wharf or breakwater. In view of this, the second-order wave theory was adopted in this study to investigate the wave run-up on a cylinder near a long vertical wall. The image principle was used to transfer the original problem into an equivalent one in open seas. The second-order wave run-up on the cylinder can then be determined by using the wave elevation quadratic transfer function (QTF) obtained from an analysis of the equivalent problem. Based on a numerical model proposed in this study, a detailed numerical analysis was conducted. Numerical results revealed that the wave run-up on a cylinder in front of a vertical wall behaves in an oscillatory manner around that experienced by a cylinder in open seas. A pronounced wave run-up was observed around the cylinder as well as on the vertical wall. Around the lee side of the cylinder and a region on the wall that sheltered by the cylinder, the prediction of the wave run-up based on a second-order wave theory can largely exceed that based on a linear wave theory. Even when the wave steepness is small, the second-order wave elevation component can still make an apparent correction to the wave elevation distribution in the vicinity of a cylinder situated near a vertical wall.

Following the introduction, the development of the numerical model for the second-order wave diffraction caused by an arbitrarily shaped structure in bi-directional waves is introduced in detail. Then, the validity of the proposed model is examined in the next section. Afterwards, the application of the model in the wave interaction with a cylinder situated near a vertical wall is presented, and a variety of computed results are given and discussed. Finally, the main conclusions are presented.

2. Second-order wave diffraction caused by a three-dimensional structure in bi-directional waves

2.1 Mathematical formulation

The wave diffraction caused by an arbitrarily shaped, three-dimensional structure fixed in bi-directional incident waves is considered. The incident waves propagate in water of uniform depth d. Fig. 1 shows a schematic of this problem. A Cartesian coordinate system $oxyz$ with the oxy plane in the quiescent free surface and z-axis oriented upward is employed. It is assumed that the fluid is incompressible and the flow is irrotational. Then, the fluid velocity can be expressed in terms of the velocity potential, which is governed by Laplace's equation. By means of a perturbation procedure for the velocity potential Φ, we can obtain the following:

$$\Phi = \varepsilon\Phi^{(1)} + \varepsilon^2\Phi^{(2)} + O\left(\varepsilon^3\right), \tag{1}$$

in which ε is a small parameter proportional to the wave steepness. Similarly, the wave elevation Ξ and wave force $\mathbf{F}$ can be expressed as follows:

$$\zeta = \varepsilon\zeta^{(1)} + \varepsilon^2\zeta^{(2)} + O\left(\varepsilon^3\right), \tag{2}$$

and

$$\mathbf{F} = \varepsilon\mathbf{F}^{(1)} + \varepsilon^2\mathbf{F}^{(2)} + O\left(\varepsilon^3\right). \tag{3}$$

In Eqs. (1), (2), and (3), the subscripts (1) and (2) represent the first- and second-order quantities, respectively.

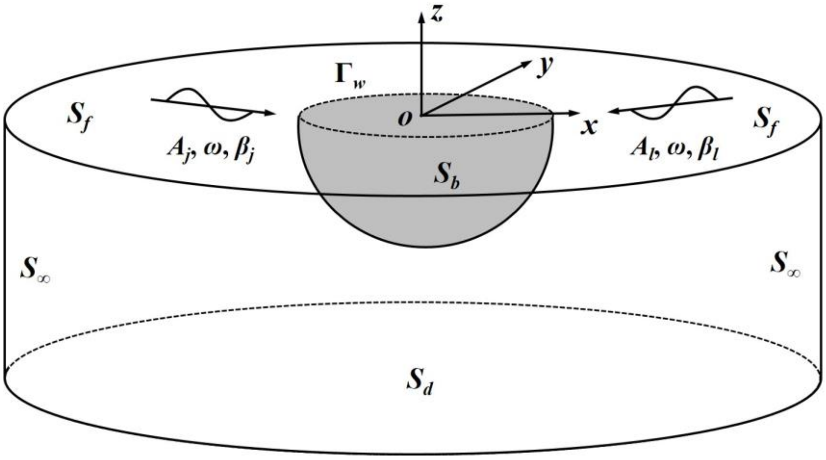

Fig. 1 Schematic of the problem of wave diffraction caused by a three-dimensional structure in bi-directional incident waves

In the presence of dual incident waves of the same frequency ω but different headings

β_1 and β_2, the total first-order velocity potential can be expressed as

$$\varepsilon\Phi^{(1)}(\mathbf{x},\ t) = \mathrm{Re}\left[\sum_{j=1}^{2}\phi_j^{(1)}(\mathbf{x})e^{-i\omega t}\right], \tag{4}$$

where Re[ ] denotes the real part of a complex expression and $\phi_j^{(1)}$ represents the first-order velocity potential due to the incident waves travelling from the jth direction. Meanwhile, the second-order velocity potential can be expressed as a summation of a double-frequency term and a time-independent term. That is,

$$\varepsilon^2\Phi^{(2)}(\mathbf{x},\ t) = \mathrm{Re}\left[\sum_{j=1}^{2}\sum_{l=1}^{2}\left(\phi_{jl}^{(2)}(\mathbf{x})e^{-2i\omega t} + \bar{\phi}_{jl}^{(2)}(\mathbf{x})\right)\right]. \tag{5}$$

In Eq. (5), $\phi_{jl}^{(2)}$ and $\bar{\phi}_{jl}^{(2)}$ represent the double-frequency and the time-independent terms, respectively, which are related to the interaction between the jth and lth wave components. The steady term $\bar{\phi}_{jl}^{(2)}$ is subsequently neglected, as it does not contribute to the second-order wave run-up or wave force. $\phi_j^{(1)}$ and $\phi_{jl}^{(2)}$ can be further decomposed as a summation of the incident potential and the diffraction potential. That is,

$$\phi_j^{(1)}(\mathbf{x}) = \phi_{j,\,I}^{(1)}(\mathbf{x}) + \phi_{j,\,D}^{(1)}(\mathbf{x}), \quad j = 1,\ 2; \tag{6a}$$

$$\phi_{jl}^{(2)}(\mathbf{x}) = \phi_{jl,\,I}^{(2)}(\mathbf{x}) + \phi_{jl,\,D}^{(2)}(\mathbf{x}), \quad j,\ l = 1,\ 2. \tag{6b}$$

The incident potentials $\phi_{j,\,I}^{(1)}$ and $\phi_{jl,\,I}^{(2)}$ have been derived in some previous studies, for instance, Kim (1993) and Mei et al. (2005). The expression for $\phi_{j,\,I}^{(1)}$ is given by

$$\phi_{j,\,I}^{(1)}(\mathbf{x}) = -\frac{iA_j g}{\omega}\frac{\cosh k(z+d)}{\cosh kd}e^{ik\left(x\cos\beta_j + y\sin\beta_j\right)}, \quad j = 1,\ 2, \tag{7}$$

in which A_j is the amplitude of the jth component of the incident waves, and the wavenumber k is related to the wave frequency ω through a dispersion relation: $\omega^2 = gk\tanh kd$. The expression for $\phi_{jl,\,I}^{(2)}$ is then given by

$$\phi_{jl,\,I}^{(2)}(\mathbf{x}) = -\frac{iA_j A_l g}{2\omega}\frac{C_{jl}^{+}}{D_{jl}^{+}}\frac{\cosh k_{jl}^{+}(z+d)}{\cosh k_{jl}^{+}d}e^{ik\left[x\left(\cos\beta_j+\cos\beta_l\right)+y\left(\sin\beta_j+\sin\beta_l\right)\right]}, \tag{8}$$

where C_{jl}^{+}, D_{jl}^{+}, and k_{jl}^{+} are defined by

$$C_{jl}^{+} = k^2\left[1 + 2\cos\left(\beta_j - \beta_l\right) - 3\tanh^2 kd\right]; \tag{9a}$$

$$D_{jl}^{+} = \left(4\omega^2 - gk_{jl}^{+} \tanh k_{jl}^{+} d\right) / g; \tag{9b}$$

$$k_{jl}^{+} = k\sqrt{2 + 2\cos\left(\beta_j - \beta_l\right)}. \tag{9c}$$

As β_j approaches β_l, the second-order incident velocity potential given by Eq. (8) can be reduced to the form of the second-order Stokes waves.

We then turn to the solution of the first- and second-order diffraction potentials, that is, $\phi_{j,D}^{(1)}$ and $\phi_{jl,D}^{(2)}$. The boundary value problem at each order is subsequently formulated with respect to a fluid domain bounded by the seabed, the body surface, the still water surface, and a surface located sufficiently far from the body. The boundary conditions satisfied by $\phi_{j,D}^{(1)}$ can be written as follows:

$$\frac{\partial \phi_{j,D}^{(1)}}{\partial n} = -\frac{\partial \phi_{j,I}^{(1)}}{\partial n}, \quad \text{on } S_b; \tag{10a}$$

$$\frac{\partial \phi_{j,D}^{(1)}}{\partial z} = \frac{\omega^2}{g}\phi_{j,D}^{(1)}, \quad \text{on } z = 0; \tag{10b}$$

$$\frac{\partial \phi_{j,D}^{(1)}}{\partial z} = 0, \quad \text{on } z = -d. \tag{10c}$$

In Eq. (10a), S_b represents the body surface, and $\mathbf{n}$ is the normal vector on S_b pointing out of the fluid. In addition, $\phi_{j,D}^{(1)}$ needs to satisfy the Sommerfeld radiation condition at the far field.

The boundary conditions for $\phi_{jl,D}^{(2)}$ are given as

$$\frac{\partial \phi_{jl,D}^{(2)}}{\partial n} = -\frac{\partial \phi_{jl,I}^{(2)}}{\partial n}, \quad \text{on } S_b; \tag{11a}$$

$$\frac{\partial \phi_{jl,D}^{(2)}}{\partial z} = \frac{4\omega^2}{g}\phi_{jl,D}^{(2)} + \frac{1}{g}Q_{jl}^{(2)}(\mathbf{x}), \quad \text{on } z = 0; \tag{11b}$$

$$\frac{\partial \phi_{jl,D}^{(2)}}{\partial z} = 0, \quad \text{on } z = -d. \tag{11c}$$

In Eq. (11b), $Q_{jl}^{(2)}$ is the free-surface forcing term. In the presence of monochromatic bi-directional incident waves, the expression for $Q_{jl}^{(2)}$ is given by

$$Q_{jl}^{(2)}(\mathbf{x}) = i\omega\left(\nabla\phi_j^{(1)}\cdot\nabla\phi_l^{(1)} - \nabla\phi_{j,I}^{(1)}\cdot\nabla\phi_{l,I}^{(1)}\right)$$
$$+\frac{i\omega}{2}\left[\frac{\omega^4}{g^2}\left(\phi_j^{(1)}\phi_l^{(1)} - \phi_{j,I}^{(1)}\phi_{l,I}^{(1)}\right) - \frac{1}{2}\frac{\partial^2\phi_j^{(1)}}{\partial z^2}\phi_l^{(1)} - \frac{1}{2}\phi_j^{(1)}\frac{\partial^2\phi_l^{(1)}}{\partial z^2} + k^2\phi_{j,I}^{(1)}\phi_{l,I}^{(1)}\right]. \quad (12)$$

The far-field behaviour of $\phi_{jl,D}^{(2)}$ in the bi-directional problem is then examined. Following the work by Molin (1979), $\phi_{jl,D}^{(2)}$ can be decomposed into a homogeneous (free waves) solution, $\phi_{jl,H}^{(2)}$, and a particular (locked waves) solution, $\phi_{jl,P}^{(2)}$, at a large distance from the structure. That is,

$$\phi_{jl,D}^{(2)} = \phi_{jl,H}^{(2)} + \phi_{jl,P}^{(2)}. \quad (13)$$

On the undisturbed free surface, we can have

$$\frac{\partial\phi_{jl,H}^{(2)}}{\partial z} = \frac{4\omega^2}{g}\phi_{jl,H}^{(2)}, \quad \text{on } z = 0; \quad (14a)$$

$$\frac{\partial\phi_{jl,P}^{(2)}}{\partial z} = \frac{4\omega^2}{g}\phi_{jl,P}^{(2)} + \frac{1}{g}Q_{jl}^{(2)}(\mathbf{x}), \quad \text{on } z = 0. \quad (14b)$$

$\phi_{jl,H}^{(2)}$ satisfies a homogeneous boundary condition at the free surface. At the far field, an asymptotic expression of $\phi_{jl,H}^{(2)}$ can be derived as

$$\phi_{jl,H}^{(2)} = \frac{f_{H,jl}}{\sqrt{r}}\cosh\kappa(z+d)e^{i\kappa r} + O\left(r^{-3/2}\right), \quad r\to+\infty, \quad (15)$$

where κ satisfies $4\omega^2 = g\kappa\tanh\kappa d$, $r=\sqrt{x^2+y^2}$. $f_{H,jl}$ describes the variation of the homogeneous solution around the circumferential direction at the far field. The far-field behaviour of $\phi_{jl,P}^{(2)}$ is governed by that of the free-surface forcing term $Q_{jl}^{(2)}$. $Q_{jl}^{(2)}$ contains quadratic products due to the first-order diffraction potential $\phi_{j,D}^{(1)}$ itself as well as those due to $\phi_{j,D}^{(1)}$ and non-diminishing $\phi_{j,I}^{(1)}$. Using the asymptotic expansion of the first-order velocity potential for a large argument, it is obtained that the quadratic products due to $\phi_{j,D}^{(1)}$ itself decay as $O(1/r)$ when $r \to +\infty$. Meanwhile, the quadratic products due to $\phi_{j,D}^{(1)}$ and $\phi_{j,I}^{(1)}$ decay as $O(1/r^{1/2})$ when $r \to +\infty$ and dominate the far-field behaviour of $Q_{jl}^{(2)}$. Then, we can have the following asymptotic form for $\phi_{jl,P}^{(2)}$:

$$\phi_{jl,P}^{(2)} = \frac{f_{P,jl}}{\sqrt{r}} e^{ikr\left[1+\cos\left(\theta-\theta_j\right)\right]} \cosh\left[k\sqrt{2+2\cos\left(\theta-\theta_j\right)}\left(z+h\right)\right]$$
$$+\frac{f_{P,lj}}{\sqrt{r}} e^{ikr\left[1+\cos\left(\theta-\theta_l\right)\right]} \cosh\left[k\sqrt{2+2\cos\left(\theta-\theta_l\right)}\left(z+h\right)\right]+O\left(r^{-1}\right), \quad r\to\infty. \tag{16}$$

In Eq. (16), $f_{P,jl}$ and $f_{P,lj}$ are functions depending on the variation of the particular solution around the circumferential direction at the far field. Eq. (16) satisfies Laplace's equation to the leading order as well as the boundary condition on the seabed. Eqs. (13), (15), and (16) suggest that $\phi_{jl,D}^{(2)}$ decays as $O(1/r^{1/2})$ at the far field. Then, a weak radiation condition can be guaranteed for $\phi_{jl,D}^{(2)}$ in the bi-directional problem.

2.2 Boundary integral equation method for the diffraction potential

The boundary integral equation method is adopted in the present study to solve the established boundary value problem, as it explicitly takes advantage of reducing the dimension of the problem by one order. The oscillating source, which satisfies the linear free-surface boundary condition, the no-flow condition on the horizontal seabed, and the Sommerfeld radiation condition at infinity, is used as Green's function. The use of the classical Green's second identity to the diffraction potential and Green's function can lead to a Fredholm integral equation of the second kind for $\phi_{j,D}^{(1)}$ and $\phi_{jl,D}^{(2)}$. In addition, by using the method of stationary phase in conjunction with the asymptotic results in Eqs. (15) and (16), the integral over the far field vanishes. Then, the resulting boundary integral equation for $\phi_{j,D}^{(1)}$ and $\phi_{jl,D}^{(2)}$ can be expressed as

$$\alpha\phi_{j,D}^{(1)}\left(\mathbf{x}_0\right)-\iint_{S_b}\frac{\partial G\left(\mathbf{x},\ \mathbf{x}_0;\ \omega\right)}{\partial n}\phi_{j,D}^{(1)}\left(\mathbf{x}\right)ds=\iint_{S_b}G\left(\mathbf{x},\ \mathbf{x}_0;\ \omega\right)\frac{\partial\phi_{j,I}^{(1)}\left(\mathbf{x}\right)}{\partial n}ds; \tag{17a}$$

$$\alpha\phi_{jl,D}^{(2)}\left(\mathbf{x}_0\right)-\iint_{S_b}\frac{\partial G\left(\mathbf{x},\ \mathbf{x}_0;\ 2\omega\right)}{\partial n}\phi_{jl,D}^{(2)}\left(\mathbf{x}\right)ds$$
$$=\iint_{S_b}G\left(\mathbf{x},\ \mathbf{x}_0;\ 2\omega\right)\frac{\partial\phi_{jl,I}^{(2)}\left(\mathbf{x}\right)}{\partial n}ds-\frac{1}{g}\iint_{S_f}G\left(\mathbf{x},\ \mathbf{x}_0;\ 2\omega\right)Q_{jl}^{(2)}\left(\mathbf{x}\right)ds, \tag{17b}$$

where α is a measure of the normalised solid angle and depends on the local shape of the body surface, $\mathbf{x}$ and $\mathbf{x}_0$ are the source and field points, respectively, and S_f

represents the entire mean free surface outside the body.

The higher-order boundary element method (Teng and Eatock Taylor, 1995) is used to solve Eq. (17). The body surface is discretised into a set of curved quadrilateral or triangular elements. The body surface is smooth, and the variation of the physical quantities over the body surface is also continuous. Eq. (17) is then transferred to a system of linear algebraic equations based on isoperimetric-type techniques. The boundary integral equation for $\phi_{j,D}^{(2)}$ is similar to that for $\phi_{jl,D}^{(2)}$ with the addition of a free-surface integral over S_f. This integral over S_f results from the nonhomogeneous forcing term on the free surface (see Eq. 11(b)), which oscillates rapidly and decays slowly in amplitude with an increase in the distance from the body. To overcome this computational difficulty, the entire free surface is divided into three regions in this study, and the integral within each region is treated differently. The first region is a near-field region surrounding the structure. It is bounded by the waterline and a circular exterior boundary. Within the first region, the free surface is discretised into planar panels, and the integration is performed numerically by means of a Gaussian quadrature formula. In the middle region, the velocity potential and Green's function are expanded into a Fourier series with respect to the polar angle θ, and the free surface integral is simplified into a series of radial integrals that can be integrated numerically. In the outermost region, the integral is transformed to another form together with some residuals. By using the asymptotic expansions of Hankel functions, the new integral is further reduced to one whose integrand is represented by the summation of polynomials of various orders, and the integration of each term of the polynomials can be calculated analytically. This numerical algorithm has been successfully applied in the analysis of second-order unidirectional problems, e.g. by Eatock and Chau (1992), Sun et al. (2010), and Cong et al. (2012). The application of this method has been extended to cases of bi-directional waves in the present study.

2.3 Expression for the wave force and wave elevation QTFs

The fluid pressure can be determined based on Bernoulli's equation after obtaining the solution of the velocity potential. The hydrodynamic wave force acting on a body can then be calculated by integrating the pressure over the body surface. The complete formulation of the second-order wave force on a stationary body has been presented by, for instance, Ogilvie (1983) and Chen (2007). In the presence of monochromatic incident waves, the second-order wave force $\mathbf{F}^{(2)}$ can be expressed as the sum of a time oscillatory term and a mean term. That is,

$$\varepsilon^2\mathbf{F}^{(2)} = \mathrm{Re}\left[\mathbf{f}^{(2)}e^{-2i\omega t}\right]+\mathbf{f}_m^{(2)}, \tag{18}$$

where $\mathbf{f}^{(2)}$ and $\mathbf{f}_m^{(2)}$ represent the double-frequency and time-independent terms, respectively. $\mathbf{f}^{(2)}$ and $\mathbf{f}_m^{(2)}$ are both proportional to the products of the incident wave amplitude. Thus, $\mathbf{f}^{(2)}$ and $\mathbf{f}_m^{(2)}$ can be further written as follows:

$$\mathbf{f}^{(2)} = \sum_{j=1}^{2}\sum_{l=1}^{2}\left(A_jA_l\mathbf{f}_{jl}\right);\quad \mathbf{f}_m^{(2)} = \sum_{j=1}^{2}\sum_{l=1}^{2}\left(A_jA_l^*\mathbf{f}_{jl,\,m}\right), \tag{19}$$

in which

$$\mathbf{f}_{jl} = \left(2i\omega\rho\iint_{S_b}\phi_{jl}^{(2)}\mathbf{n}ds - \frac{\rho}{4}\iint_{S_b}\nabla\phi_j^{(1)}\cdot\nabla\phi_l^{(1)}\mathbf{n}ds - \frac{\rho}{4}\frac{\omega^2}{g}\oint_{\Gamma_w}\phi_j^{(1)}\phi_l^{(1)}\frac{\mathbf{n}}{\sqrt{1-n_3^2}}dl\right)\Big/\left(A_jA_l\right); \tag{20a}$$

$$\mathbf{f}_{jl,\,m} = \mathrm{Re}\left[\left(-\frac{\rho}{4}\iint_{S_b}\nabla\phi_j^{(1)}\cdot\nabla\phi_l^{(1)*}\mathbf{n}ds + \frac{\rho}{4}\frac{\omega^2}{g}\oint_{\Gamma_w}\phi_j^{(1)}\phi_l^{(1)*}\frac{\mathbf{n}}{\sqrt{1-n_3^2}}dl\right)\Big/\left(A_jA_l^*\right)\right]. \tag{20b}$$

In Eqs. (19) and (20), $\mathbf{f}_{jl}$ and $\mathbf{f}_{jl,\,m}$ are the double-frequency and the mean drift wave force due to the action of two incident waves of unit amplitude with headings β_j and β_l, respectively. Conventionally, $\mathbf{f}_{jl}$ and $\mathbf{f}_{jl,\,m}$ are defined as the double-frequency and the mean drift wave force QTF, respectively. In the presence of monochromatic bi-directional incident waves, the following symmetry relation is satisfied by the wave force QTF:

$$\mathbf{f}_{jl} = \mathbf{f}_{lj};\quad \mathbf{f}_{jl,\,m} = \mathbf{f}_{lj,\,m}. \tag{21}$$

Meanwhile, after getting the velocity potential, the wave elevation can also be immediately obtained. The first- and second-order wave elevations, that is, $\zeta^{(1)}$ and $\zeta^{(2)}$, have the following forms:

$$\varepsilon\zeta^{(1)} = \mathrm{Re}\left[\eta^{(1)}e^{-i\omega t}\right]; \tag{22a}$$

$$\varepsilon^2\zeta^{(2)} = \mathrm{Re}\left[\eta^{(2)}e^{-2i\omega t}\right] + \eta_m^{(2)}, \tag{22b}$$

where $\eta^{(1)}$ is the amplitude of the linear wave elevation, $\eta^{(2)}$ is the amplitude of the double-frequency wave elevation, $\eta_m^{(2)}$ and is the time-independent wave elevation. Under the action of monochromatic bi-directional incident waves, $\eta^{(1)}$ can be determined according to the following expression:

$$\eta^{(1)} = \frac{i\omega}{g}\sum_{j=1}^{2}\phi_j^{(1)}\bigg|_{z=0}. \tag{23}$$

Meanwhile, $\eta^{(2)}$ and $\eta_m^{(2)}$ can be expressed as follows:

$$\eta^{(2)} = \sum_{j=1}^{2}\sum_{l=1}^{2}\left(A_jA_l\eta_{jl}\right); \quad \eta_m^{(2)} = \sum_{j=1}^{2}\sum_{l=1}^{2}\left(A_jA_l^*\eta_{jl,\,m}\right), \tag{24}$$

in which

$$\eta_{jl} = \left(\frac{2i\omega}{g}\phi_{jl}^{(2)} - \frac{1}{4g}\nabla\phi_j^{(1)}\cdot\nabla\phi_l^{(1)} - \frac{v^2}{2g}\phi_j^{(1)}\phi_l^{(1)}\right)\Big/\left(A_jA_l\right)\bigg|_{z=0}; \tag{25a}$$

$$\eta_{jl,\,m} = \mathrm{Re}\left[\left(-\frac{1}{4g}\nabla\phi_j^{(1)}\cdot\nabla\phi_l^{(1)*} + \frac{v^2}{2g}\phi_j^{(1)}\phi_l^{(1)*}\right)\Big/\left(A_jA_l^*\right)\bigg|_{z=0}\right]. \tag{25b}$$

In Eq. (25), v is the deep-water wavenumber and is defined as ω^2/g; η_{jl} and $\eta_{jl,\,m}$ represent the double-frequency and the time-independent wave elevations due to the action of two incident waves of unit amplitude with headings β_j and β_l, respectively. Conventionally, η_{jl} and $\eta_{jl,\,m}$ are defined as the double-frequency and time-independent wave elevation QTF, respectively. In the presence of monochromatic bi-directional incident waves, the following symmetry relation is obtained:

$$\eta_{jl} = \eta_{lj}; \quad \eta_{jl,\,m} = \eta_{lj,\,m}. \tag{26}$$

3. Convergence test and validation

To verify the reliability of the present results, the convergence of such results with respect to the mesh discretisation is examined. A pair of vertical cylinders of radius a in water of depth $4a$ is first taken as an example. The centres of the cylinders are located at ($\pm 2.5a$, 0) on the quiescent free surface. In addition, the wave headings β_j and β_l are equal to $\pi/4$ and 0, respectively. A numerical calculation is carried out to evaluate the double-frequency wave force on the x- and y-directions on the upstream cylinder (whose centre is located at $(-2.5a, 0)$ on the quiescent free surface). In the calculation, two geometric symmetry planes are adopted to facilitate the computation. Two discretisations are employed to test the convergence of the results. In the first case, 1538 quadrilateral elements are used in each quadrant (520 elements on the body surface and 1018 elements in the near-field water plane area with an exterior radius of $9a$). In the second case, 3329 quadrilateral elements are used in each quadrant (1140 elements on the body surface and 2189 elements in the near-field water plane area with an exterior radius equal to $12a$). The mesh discretisations in the two test cases are depicted in Fig. 2. In Fig. 3, the wave force QTF on the upstream cylinder is plotted as a function of νa. For comparison, the results reported by Vazquez (1995) are also presented in Fig. 3. Considering the effect of the wave directionality, Vazquez (1995) developed a numerical model to predict the second-order wave force on a pair of cylinders based on an indirect method (Lighthill, 1979; Molin, 1979). The indirect method has been proved to be efficient in calculating the wave force. However, because no solution is obtained for the diffraction potential, it is not possible to obtain solutions of the wave elevation by using the indirect method. From Fig. 3, it is found that the present results are in good agreement with those of the study by Vazquez (1995). In addition, even though the mesh in the first case is much coarser than that in the second case, the two test cases provide almost the same results, which indicates that convergence is achieved.

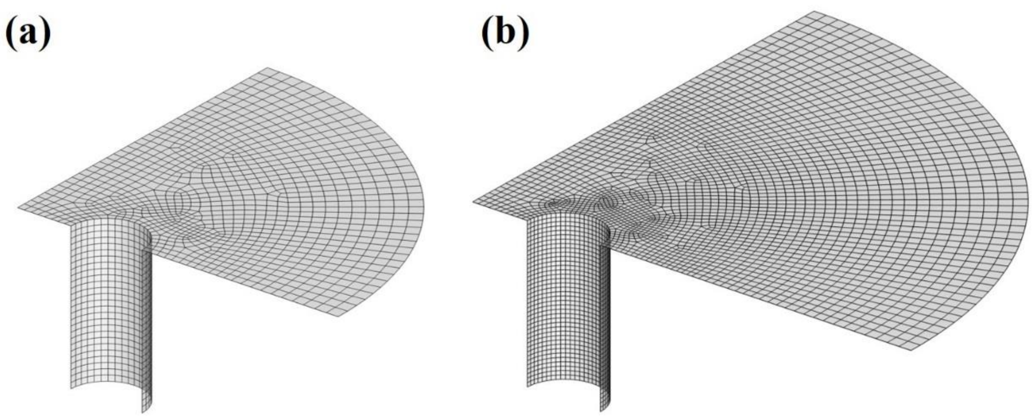

Fig. 2 Mesh discretisation on the body surface and near-field free surface in a quarter area: (a) first test case and (b) second test case

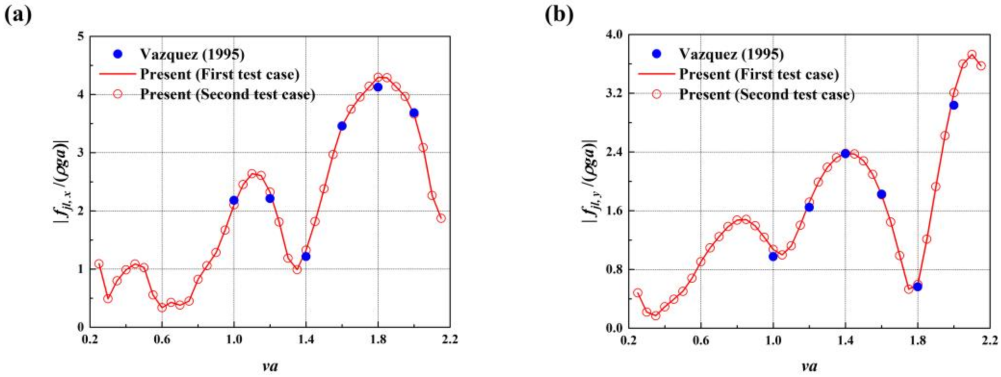

Fig. 3 Comparison of the dimensionless double-frequency wave force QTF on the upstream cylinder of a pair of vertical cylinders with $\beta_j = \pi/4$ and $\beta_l = 0$: (a) $f_{jl,\,x}$ and (b) $f_{jl,\,y}$

We then consider the wave interaction with four identical vertical cylinders, which are with radius a and centred at the corners of a square with a side length of $4a$. The centres of the cylinders are located at ($\pm 2a$, $\pm 2a$) on the quiescent free surface, and the cylinders are numbered anticlockwise with cylinder 1 located in the first quadrant. A local coordinate system is defined at each cylinder with the origin at the centre of the cylinder, and the local axis is parallel to the axis of the global coordinate system. Unidirectional incident waves with $\beta_j = \beta_l = \pi/4$ and $A_j = A_l = A$ are considered. The water depth d is equal to $3a$. This set-up is the same as that in the study by Malenica et al. (1999), in which a semi-analytical solution to the second-order wave diffraction caused by an array of vertical cylinders was developed. The present results of the wave elevation QTF are then compared with the semi-analytical results. In the calculation, 1906 quadrilateral elements are used in each quadrant (800 elements on the body surface and 1106 elements in the near-field water plane area with an outer radius of $9a$). The comparison is shown in Fig. 4. It is apparent that there is good agreement between the present results and the semi-analytical results, which further confirms the validity of the present model.

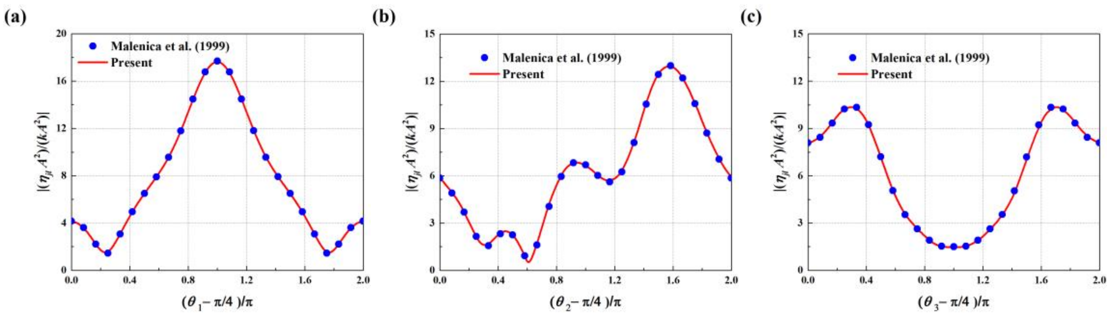

Fig. 4 Comparison of the dimensionless double-frequency wave elevation QTF on a four-cylinder structure with $\beta_j = \beta_l = \pi/4$ and $ka = 0.468$: (a) cylinder 1, (b) cylinder 2, and (c) cylinder 3

4. Investigation of wave run-up on a cylinder in front of a vertical wall

The wave diffraction caused by a vertical circular cylinder of radius a piercing through the free surface in front of a long vertical wall is considered (see Fig. 5). The amplitude and angular frequency of the incident waves are A and ω, respectively. In addition, the distance between the wall and centre of the cylinder is R. The impermeable vertical wall extends from the seabed to the free surface and is assumed to be infinitely long and fully reflective. Then, following Teng et al. (2004), the problem described in Fig. 5 can be transformed into an equivalent problem in open seas (see Fig. 6).

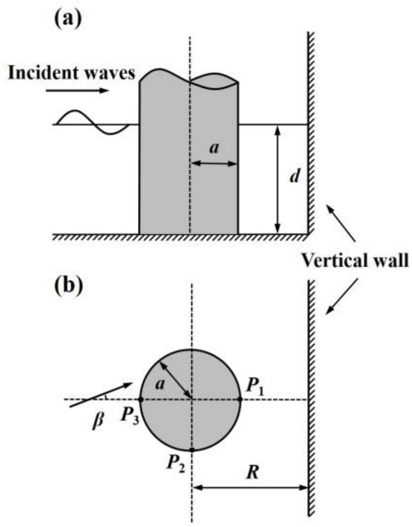

Fig. 5 Schematic of a cylinder situated near a vertical wall: (a) side view and (b) plan view

The illustration of the equivalent problem in open seas and the definition of the Cartesian coordinate system *oxyz* in an imaginary system are depicted in Fig. 6. As shown, the quiescent free surface is on the *oxy* plane, and the z-axis points upward. The original vertical wall is on the oyz plane, and (0, 0) is defined as the center of the wall on the free surface. In Fig. 6, the left and right cylinders are the real and imaginary cylinders, respectively. Their centres are at ($-R$, 0) and (R, 0), respectively, on the quiescent free surface. The two cylinders are subjected to two trains of monochromatic incident waves of amplitude A and angular frequency ω travelling from the directions of β and $\pi - \beta$ relative to the positive x-axis, respectively. In addition, in the subsequent calculations, a water depth of $d = 3a$ is adopted.

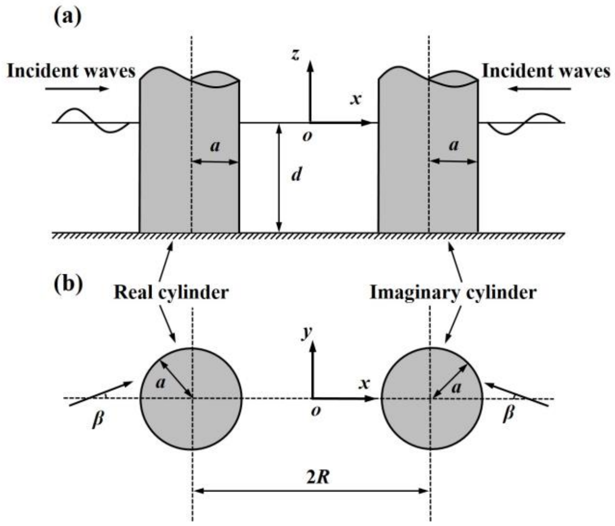

Fig. 6 Schematic of two symmetrical vertical cylinders in an imaginary system: (a) side view and (b) plan view

4.1 Wave run-up at specific points

To better elucidate the effect of the vertical wall on the wave elevation around the structure, also known as wave run-up, three points on a real cylinder, namely P_1, P_2, and P_3, are introduced as the feature points (see Fig. 5). P_1, P_2, and P_3 are all on the free surface and with the coordinates ($-R + a$, 0), ($-R$, $-a$), and ($-R - a$, 0), respectively, in the imaginary system.

After applying the image principle, the original problem exhibited in Fig. 5 under a single incident wave with a heading β is converted to that shown in Fig. 6 under dual incident waves with headings β and $\pi - \beta$ in open seas. When the incident wave headings are β and $\pi - \beta$, QTFs corresponding to wave heading combinations of (β, β),

($\pi - \beta$, β), (β, $\pi - \beta$), and ($\pi - \beta$, $\pi - \beta$) are required for the calculation of the second-order wave elevation. The double-frequency and the time-independent wave elevation QTFs at P_1, P_2, and P_3 with $R = 2.5a$ and $\beta = 0$ are presented in Table 1. Analogous results to those in Table 1, but with $R = 3a$ and $\beta = \pi/4$, are provided in Table 2. Because the wave elevation QTF satisfies the symmetry relation given by Eq. (26), the results in these tables are only presented for combinations of (β, β), ($\pi - \beta$, β), and ($\pi - \beta$, $\pi - \beta$). The effects of the distance between the wall and the cylinder as well as the wave heading are clearly observed by noting that there exist obvious differences between the wave elevation QTFs listed in Tables 1 and 2. It is also found that at each wave frequency, the contribution from the QTF corresponding to the combinations of (β, β), ($\pi - \beta$, β), or ($\pi - \beta$, $\pi - \beta$) to the wave elevation can be equally important. Acceptable results cannot be achieved by neglecting any of them.

Table 1 Dimensionless double-frequency and time-independent wave elevation QTF, $\left|\left(\eta_{jl}A^2\right)/\left(kA^2\right)\right|$ and $\left(\eta_{jl,\,m}A^2\right)/\left(kA^2\right)$, at P_1, P_2 and P_3 for different wave frequencies with $R = 2.5a$ and $\beta = 0$. The values shown for each heading combination are: first row, P_1; second-row, P_2; third row, P_3.

(a) Double-frequency wave elevation QTF

ka / (β_j, β_l)	0.6	0.9	1.2	1.5	1.8
	3.525	2.487	1.445	0.892	0.433
(β, β)	3.107	1.192	1.931	1.229	1.409
	0.549	1.070	0.814	0.623	0.740
	3.619	0.622	1.008	0.121	0.543
($\pi - \beta$, β)	2.565	0.433	0.759	0.136	0.699
	1.667	1.080	0.570	0.568	0.371
	3.543	2.171	1.893	1.068	1.443
($\pi - \beta$, $\pi - \beta$)	2.556	1.052	0.921	1.166	0.402
	2.360	1.241	1.184	0.435	0.421

(b) Time-independent wave elevation QTF

ka / (β_j, β_l)	0.6	0.9	1.2	1.5	1.8

	0.205	0.105	0.481	0.296	0.031
(β, β)	−1.227	0.006	−0.630	0.392	−0.316
	0.762	0.565	0.807	0.744	0.928
	0.284	−0.199	−0.564	−0.420	−0.131
$(\pi - \beta, \beta)$	−1.335	−0.002	0.935	0.004	0.740
	0.248	0.086	−0.332	0.295	−0.111
	0.559	0.630	0.757	0.614	0.557
$(\pi - \beta, \pi - \beta)$	−0.719	−0.340	−0.094	0.029	−0.009
	0.222	0.185	0.173	0.118	0.096

Table 2 Dimensionless double-frequency and time-independent wave elevation QTF, $\left|(\eta_{jl}A^2)/(kA^2)\right|$ and $(\eta_{jl,m}A^2)/(kA^2)$, at P_1, P_2 and P_3 for different wave frequencies with $R = 3a$ and $\beta = \pi/4$. The values shown for each heading combination are: first row, P_1; second-row, P_2; third row, P_3.

(a) Double-frequency wave elevation QTF

ka / (β_j, β_l)	0.6	0.9	1.2	1.5	1.8
	1.089	2.370	1.909	1.601	1.103
(β, β)	1.046	0.523	0.659	0.657	1.199
	0.623	0.645	0.608	0.503	0.924
	1.531	1.253	1.135	0.484	0.842
$(\pi - \beta, \beta)$	1.051	0.366	0.559	0.424	0.656
	1.394	1.196	1.000	1.018	0.615
	0.781	2.013	1.908	0.783	1.128
$(\pi - \beta, \pi - \beta)$	1.221	1.216	0.493	1.339	0.937
	1.741	1.837	1.541	1.286	0.965

(b) Time-independent wave elevation QTF

ka / (β_j, β_l)	0.6	0.9	1.2	1.5	1.8
	−0.507	−0.432	−0.274	−0.427	−0.161
(β, β)	−0.049	0.373	0.187	0.642	−0.253
	0.083	0.196	0.472	0.178	0.374
	0.271	0.078	0.148	0.292	0.367
$(\pi - \beta, \beta)$	−0.625	−0.809	0.329	1.250	−0.031
	0.399	−0.045	0.016	0.121	−0.023
	−0.184	0.255	0.163	0.369	0.772
$(\pi - \beta, \pi - \beta)$	0.095	0.309	0.291	0.315	0.298
	−0.548	−0.438	−0.376	−0.280	−0.272

Based on the QTF results, the second-order wave run-up at P_1, P_2, and P_3 can then be determined. The variation of the wave run-up at P_1, P_2, and P_3 with respect to ka is shown in Figs. 7–12. In order to achieve a better understanding, the results of the linear wave run-up are also presented in the figures. In addition, in these figures, the results referred to as 'UW' correspond to those of a single cylinder in open seas.

The effect of the distance between the wall and the cylinder on the wave run-up at P_1, P_2, and P_3 is illustrated in Figs. 7–9. In the calculations, β is fixed at 0, and R is varied as $R = 2a$, $2.5a$, and $3a$. From Figs. 7–9, strong evidence of the pronounced effect of the vertical wall on the wave diffraction process is observed. In Fig. 7, the linear wave run-up amplitude on a cylinder situated near a vertical wall oscillates around that experienced by a cylinder in open seas. Obvious amplification of the linear wave run-up can be observed due to the influence of the vertical wall. When $R = 2a$, a linear wave run-up that exceeds 3 times the incident wave amplitude can be observed at P_1 (see Fig. 7(a)). It is also noted that, at each location, the oscillation of the wave run-up with ka becomes more frequent as R increases. In addition, for a fixed distance between the wall and cylinder, such oscillation gradually becomes more frequent from P_1 to P_2 and P_3.

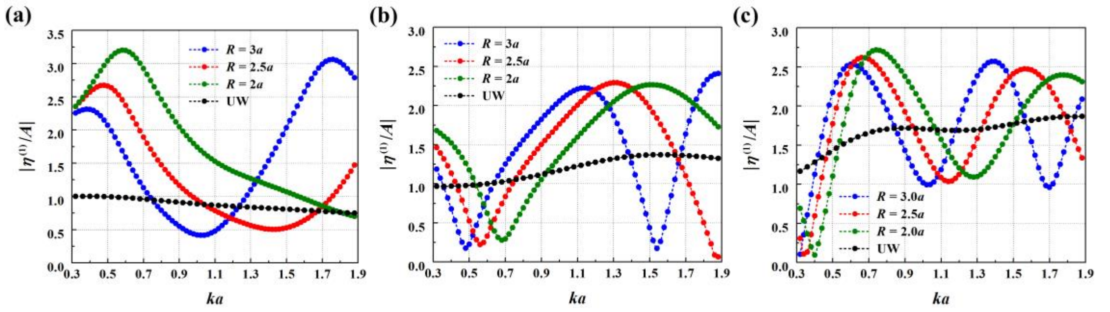

Fig. 7 Dimensionless linear wave run-up amplitudes, $\left|\eta^{(1)}/A\right|$, at (a) P_1, (b) P_2, and (c) P_3 for different distances between the wall and cylinder

Fig. 8 presents the variation of the time-independent wave run-up at P_1, P_2, and P_3 with respect to ka for different values of R. The time-independent wave run-up is obtained directly from the first-order quantities. When $\beta = 0$, owing to the symmetry of the structure, the fluid particles at P_1 and P_3 move only in the vertical direction. Then, at P_1 and P_3, the time-independent wave run-up is proportional to the square of the linear wave run-up. Therefore, the variation of the wave run-up in Figs. 8(a) and 8(c) is similar to that in Figs. 7(a) and 7(c). Moreover, the frequencies of the obvious peaks and troughs in Figs. 8(a) and 8(c) coincide with those in Figs. 7(a) and 7(c). At P_2, the fluid particle moves not only in the vertical direction but also in the horizontal plane. This can lead to discrepancies between the frequencies of the peaks and troughs in Fig. 8(b) and those in Fig. 7(b).

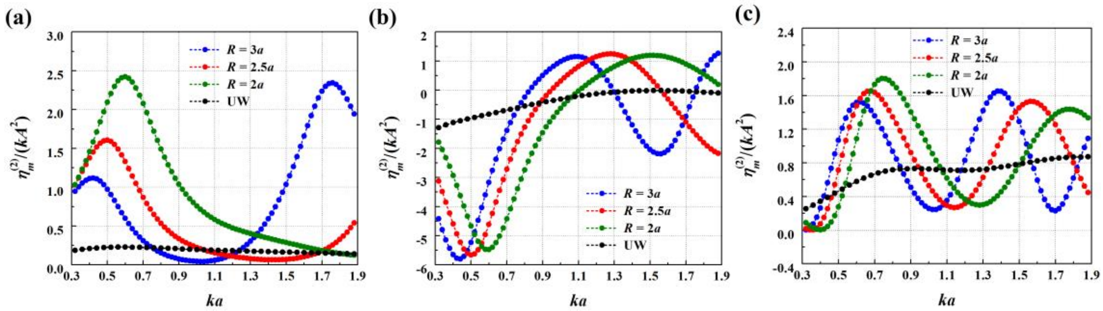

Fig. 8 Dimensionless time-independent wave run-up, $\eta_m^{(2)}/(kA^2)$, at (a) P_1, (b) P_2, and (c) P_3 for different distances between the wall and cylinder

The variation of the double-frequency wave run-up amplitude at P_1, P_2, and P_3 with respect to ka is shown in Fig. 9 for different values of R. The double-frequency wave run-up on a cylinder situated near a vertical wall also oscillates around that experienced by a vertical cylinder in open seas. Such oscillation becomes more frequent as the cylinder gets far away from the wall. The effect of the vertical wall on the double-frequency wave run-up is generally more significant than that on the linear wave run-up. Owing to the influence of the vertical wall, a greatly amplified double-frequency wave run-up can be observed in the low-frequency region. At P_1, an obvious peak with a value of 17.174 can be observed at ka = 0.48 when R = 3a. This suggests that when the wave steepness is 0.06, the double-frequency wave run-up at P_1 can reach 1.030 times the incident wave amplitude when R = 3a and ka = 0.48. As the wave steepness increases further to 0.1, it grows to 1.717 times the incident wave amplitude. Meanwhile, the corresponding linear wave run-up amplitude is 2.150 times the incident wave amplitude. Despite being a correction term, the second-order wave run-up, which is proportional to the square of the wave steepness, becomes progressively important as the wave steepness increases. The above observation typically demonstrates the significance of the second-order effect in the hydrodynamic analysis.

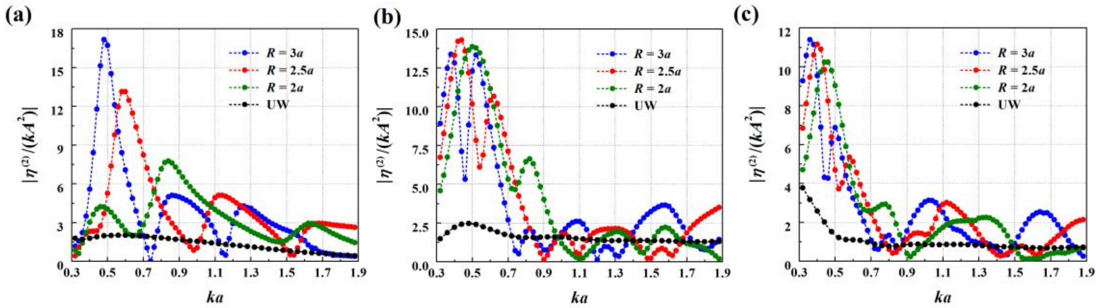

Fig. 9 Dimensionless double-frequency wave run-up amplitudes, $\left|\eta^{(2)}/\left(kA^2\right)\right|$, at (a) P_1, (b) P_2, and (c) P_3 for different distances between the wall and cylinder

The wave heading can also affect the wave run-up on the cylinder, as illustrated in Figs. 10–12. In the calculations, the distance between the wall and cylinder was fixed at $R = 3a$, and the wave heading was increased from 0 to $\pi/4$ with an interval of $\pi/12$. As shown in Fig. 10, as the wave heading increases, the oscillation of the linear wave run-up with ka becomes less frequent. As the propagation direction of the incident waves deviates from the positive x-direction, at P_1, P_2, and P_3, the motion of the fluid particle in the horizontal plane can be enhanced. Therefore, the trend of the time-independent wave run-up gradually differs from that of the linear wave run-up as β increases (see Fig. 11). In Fig. 12, the variation of the double-frequency wave run-up with respect to ka exhibits remarkable oscillations. At P_1 (see Fig. 12(a)), each curve is characterised by an obvious peak around $ka = 0.48$. The change in the wave heading does not obviously affect the frequency of the obvious peak, while the peak value decreases gradually as β increases. At P_2 and P_3 (see Figs. 12(b) and 12(c)), the appearance of two obvious peaks in the low-frequency region is noticeable, and the peak value decreases monotonically as β increases. An exception can be found at the second peak at P_2, where the case of $\beta = \pi/12$ indicates the largest peak value among different wave headings.

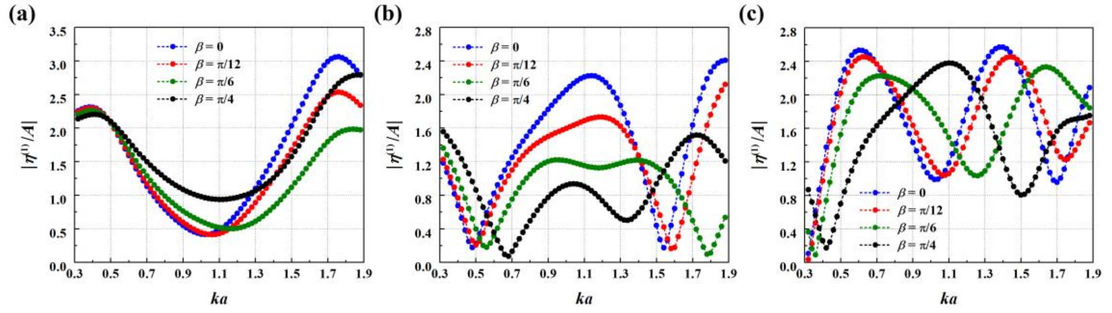

Fig. 10 Dimensionless linear wave elevation amplitudes, $\left|\eta^{(1)}/A\right|$, at (a) P_1, (b) P_2, and (c) P_3 for different incident wave headings

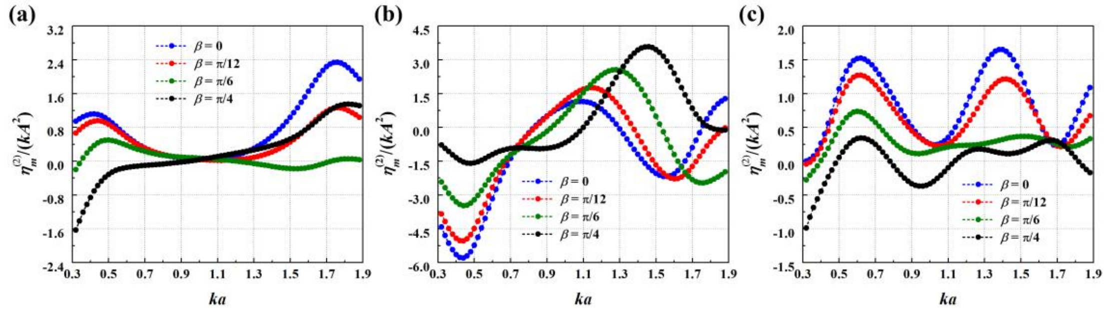

Fig. 11 Dimensionless time-independent wave elevations, $\eta_m^{(2)}/\left(kA^2\right)$, at (a) P_1, (b) P_2, and (c) P_3 for different incident wave headings

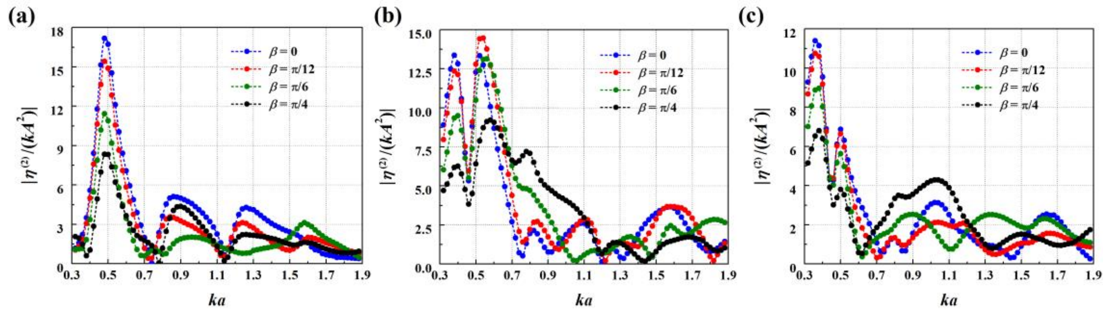

Fig. 12 Dimensionless double-frequency wave elevation amplitudes, $\left|\eta^{(2)}/\left(kA^2\right)\right|$, at (a) P_1, (b) P_2, and (c) P_3 for different incident wave headings

4.2 Wave run-up distribution around a cylinder

The effect of a vertical wall on the wave run-up distribution around a cylinder is investigated. Fig. 13 depicts the effect of the distance between the wall and cylinder on the wave run-up distribution with $\beta = 0$ and $ka = 0.48$. Fig. 13(a) shows the variation of the linear wave run-up with respect to θ, in which $\theta = \tan^{-1}\left[y/\left(x+R\right)\right]$. In Fig. (13a), obvious peaks are observed around the weather side ($\theta = \pi$) and the lee side ($\theta = 0$ or

2π), respectively. Moreover, obvious troughs, which move gradually to the lee side as *R* increases, are observed between them. It is also found that the presence of the vertical wall can amplify the linear wave run-up around the lee side. In Fig. 13(b), the variation of the time-independent wave run-up on the cylinder is similar to that in Fig. 13(a), and the presence of the vertical wall clearly reinforces the negative time-independent wave run-up on the cylinder. In Fig. 13(c), the double-frequency wave run-up varies rapidly on the cylinder. In addition, it is interesting to find that regardless of the value of *R*, the presence of the vertical wall can amplify the double-frequency wave run-up at almost all locations on the cylinder.

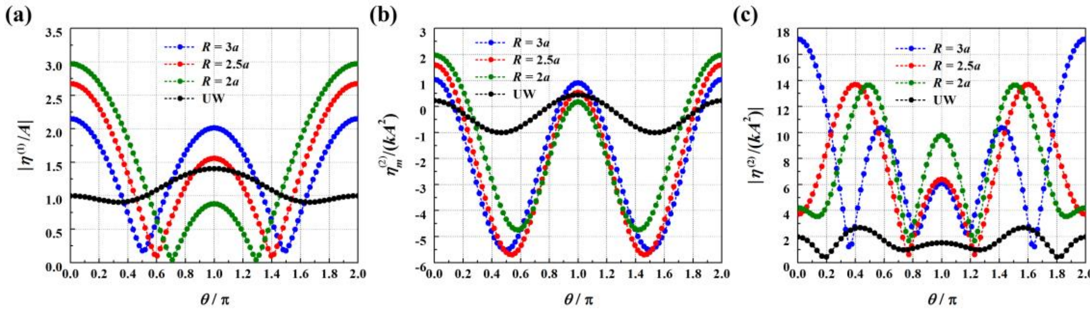

Fig. 13 Wave run-up on a cylinder situated near a wall at ka = 0.48 for different distances between the wall and cylinder: (a) $\left|\eta^{(1)}/A\right|$, (b) $\eta_m^{(2)}/\left(kA^2\right)$, and (c) $\left|\eta^{(2)}/\left(kA^2\right)\right|$

The variation of the wave run-up around a cylinder for different wave headings is presented in Fig. 14 with $R = 3a$ and $ka = 0.48$. When $\beta > 0$, the distribution of the wave run-up around the cylinder is no longer symmetrical about the *x*-axis. As shown in Fig. 14(a), the wave heading has a negligible effect on the wave run-up amplitude around $\theta = 0$ (or 2π), while that around $\theta = \pi$ continues to decrease as β increases. Moreover, in Fig. 14(a), the obvious troughs move gradually to the weather side as β increases. As indicated in Fig. 14(b), the time-independent wave run-up around the cylinder decays gradually in magnitude as β increases. Furthermore, from Fig. 14(c), it is also found that an increase in β can lead to a decrease in the peak wave run-up on the cylinder.

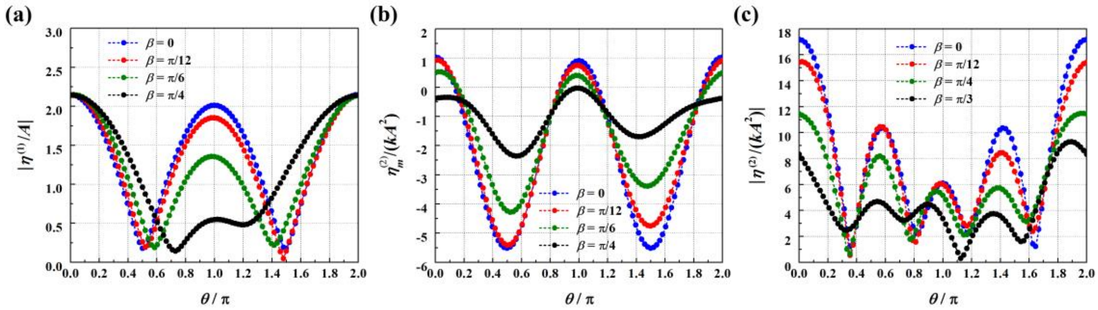

Fig. 14 Wave run-up on a cylinder situated near a wall at ka = 0.48 for different incident wave headings: (a) $\left|\eta^{(1)}/A\right|$, (b) $\eta_m^{(2)}/\left(kA^2\right)$, and (c) $\left|\eta^{(2)}/\left(kA^2\right)\right|$

Analogous results to those in Figs. 13 and 14 but with ka = 0.86 are shown in Figs. 15 and 16. The variation of the linear and the time-independent wave run-up with ka = 0.86 is different from that ka = 0.48, as an obvious trough is formed gradually at the weather side as R increases. It is also found that the double-frequency wave run-up with ka = 0.86 varies more rapidly around the cylinder than that with ka = 0.48. Even though the distribution of the wave run-up with ka = 0.86 is different from that with ka = 0.48, the effect of the vertical wall on the wave run-up is still evident at this wave frequency.

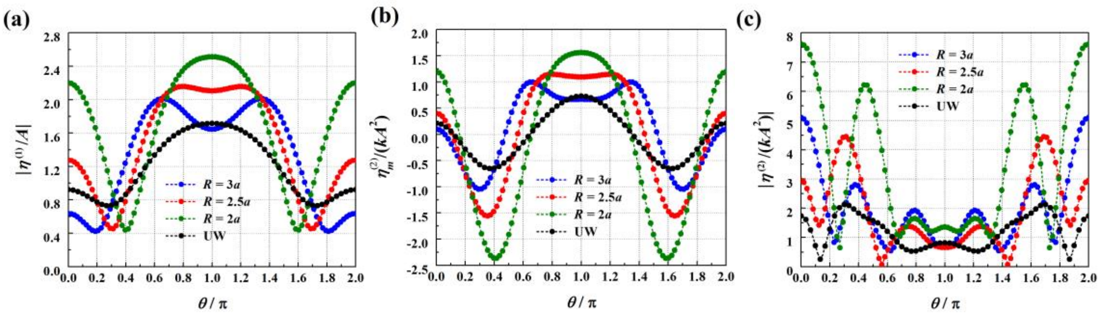

Fig. 15 Wave run-up on a cylinder situated near a wall at ka = 0.86 for different distances between the wall and cylinder: (a) $\left|\eta^{(1)}/A\right|$, (b) $\eta_m^{(2)}/\left(kA^2\right)$, and (c) $\left|\eta^{(2)}/\left(kA^2\right)\right|$

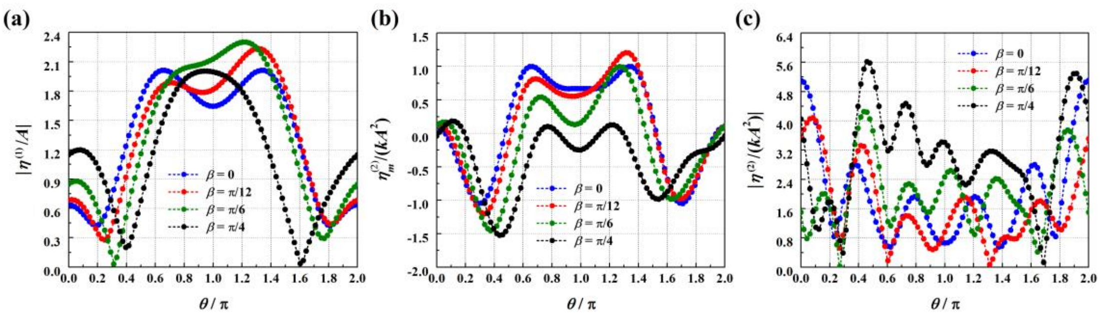

Fig. 16 Wave run-up on a cylinder situated near a wall at ka = 0.86 for different incident wave headings: (a) $\left|\eta^{(1)}/A\right|$, (b) $\eta_m^{(2)}/\left(kA^2\right)$, and (c) $\left|\eta^{(2)}/\left(kA^2\right)\right|$

4.3 Wave elevation distribution in the vicinity of a cylinder

The distribution of the overall wave elevation in the vicinity of a cylinder is then investigated. Based on the contributions from the first- and the second-order terms, the overall wave elevation to the second-order accuracy with respect to the wave steepness can be calculated according to Eq. (2). Then, the maximum and minimum overall wave elevations at a specific location, which are denoted by ζ_s and ζ_t hereinafter, can be obtained through an analysis of the wave elevation time history in a wave period. If only the first-order accuracy with respect to the wave steepness is considered, it is clear that ζ_s is equal to the amplitude of the linear wave elevation, and ζ_t is opposite to ζ_s. In the subsequent calculations, a cylinder with a dimensional radius of a = 1 m is considered, and the incident waves of ka = 0.48 and kA = 0.1 are used. The calculations of the wave elevation to the first- and second-order accuracies with respect to the wave steepness are both conducted, and the results shown in this section are all dimensional.

We first consider the situation where the cylinder is removed from the fluid domain. Then, the wave elevation is contributed by the incident waves as well as those reflected from the vertical wall. The distributions of ζ_s and ζ_t near a vertical wall in the absence of a cylinder are presented in Figs. 17 and 18 for β = 0. Because the incident waves are fully reflected from the vertical wall without transmission, a standing wave motion is observed on the wall (x = 0). If the linear wave theory is adopted, the wave elevation amplitude on the wall is 0.417 m, which is twice the incident wave amplitude. After including the second-order wave elevation component, the wave peak gets steeper, while the wave trough gets flatter, and the maximum and minimum wave elevations on the wall become 0.491 m and −0.342 m, respectively.

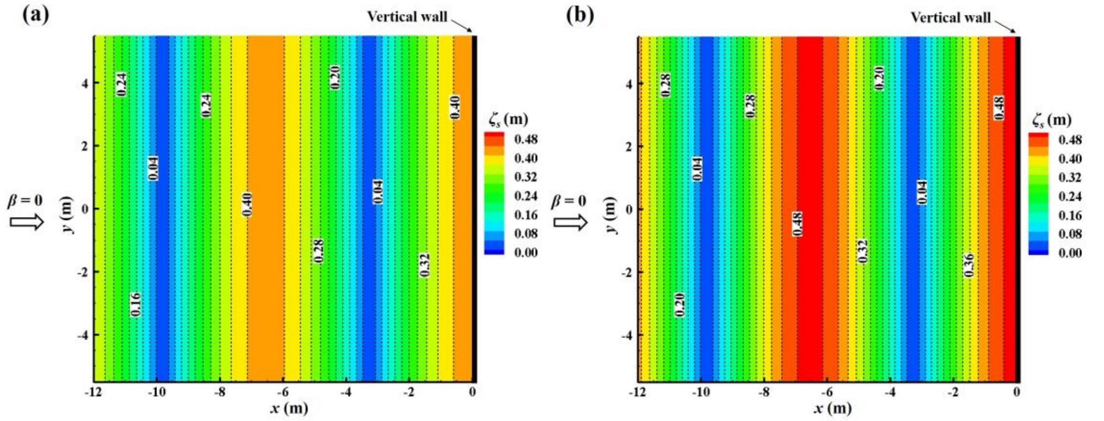

Fig. 17 Distribution of ζ_s near a wall without a cylinder at ka = 0.48 with a = 1 m, R = 3a, d = 3a, β = 0, and kA = 0.1 to the (a) first-order accuracy and (b) second-order accuracy

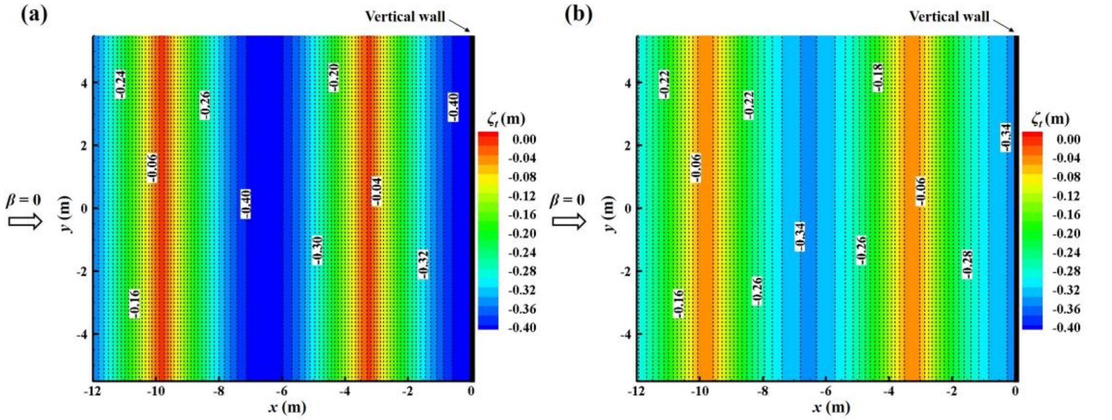

Fig. 18 Distribution of ζ_t near a wall without a cylinder at ka = 0.48 with a = 1 m, R = 3a, d = 3a, β = 0, and kA = 0.1 to the (a) first-order accuracy and (b) second-order accuracy

We then consider the wave elevation distribution in the presence of a cylinder. In Figs. 19 and 20, the distributions of ζ_s and ζ_t in the vicinity of a cylinder situated near a vertical wall are presented for $\beta = 0$ with $R = 2a$. As shown in these figures, the presence of the cylinder can obviously disturb the wave field. Pronounced wave run-up can be observed on the cylinder as well as on the wall. When $R = 2a$, the maximum wave run-up on the vertical wall appears at the centre of the wall, that is, (0, 0). In addition, on the vertical cylinder, the wave run-up at the lee side is more significant than that at the weather side, and the maximum wave run-up is attained at ($-a$, 0). If the linear wave theory is adopted, the wave run-up amplitudes at (0, 0) and ($-a$, 0) are 0.635 m and 0.619 m, respectively. After including the second-order wave elevation component, the maximum wave elevations at the two locations increase to 0.775 m and 0.740 m, respectively, and the minimum wave elevations become −0.550 m and −0.513 m, respectively. Analogous results to those in Figs. 19 and 20, but with $R = 3a$ are shown in Figs. 21 and 22. The change of the location of the cylinder can affect the relative phase between the waves around the cylinder and those reflected from the wall, and then exert an obvious influence on the wave elevation distribution around the cylinder. As the distance between the wall and the cylinder increases from $R = 2a$ to $R = 3a$, the wave run-up at the weather side of the cylinder becomes reinforced, while that at the lee side is reduced. When $R = 3a$, the maximum wave elevations on the vertical wall and the cylinder are attained at (0, 0) and ($-2a$, 0), respectively. If the linear wave theory is adopted, the wave elevation amplitudes at (0, 0) and ($-2a$, 0) are 0.541 m and 0.448 m, respectively. The effect of the second-order wave elevation component is apparent at the two locations. After including the second-order component, the maximum wave elevations at the two locations increase to 0.941 m and 0.483 m, respectively. Meanwhile, the minimum wave elevations at the two locations become −0.450 m and −0.783 m, respectively. To further emphasise the second-order effect, the time history of the overall wave elevation at (0, 0) and ($-2a$, 0) is illustrated in Fig. 23 for $\beta = 0$ with $R = 3a$. At (0, 0), the first-order and second-order double-frequency wave elevations attain their peaks at almost the same time, while at ($-2a$, 0), they attain their troughs almost simultaneously. Therefore, the maximum and minimum wave elevations at (0, 0) and ($-2a$, 0) can be obviously amplified, respectively, by including the second-order component, and the prediction based on the second-order wave theory largely exceed that based on the linear wave theory in magnitude at the two locations.

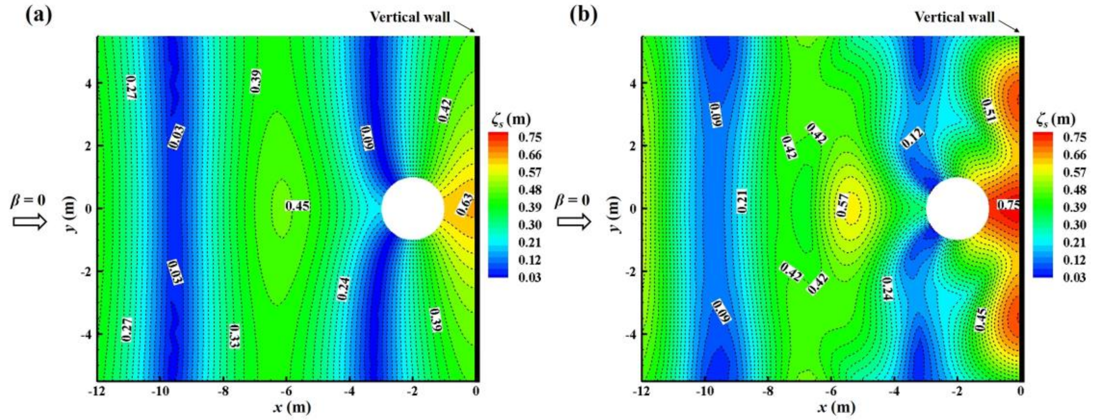

Fig. 19 Distribution of ζ_s around a cylinder situated near a wall at ka = 0.48 with a = 1 m, R = 2a, d = 3a, β = 0, and kA = 0.1 to the (a) first-order accuracy and (b) second-order accuracy

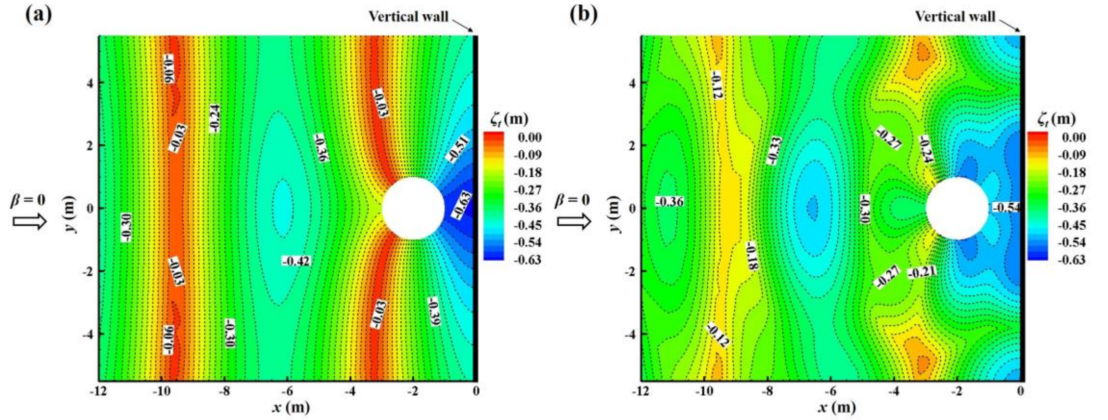

Fig. 20 Distribution of ζ_t around a cylinder situated near a wall at ka = 0.48 with a = 1 m, R = 2a, d = 3a, β = 0, and kA = 0.1 to the (a) first-order accuracy and (b) second-order accuracy

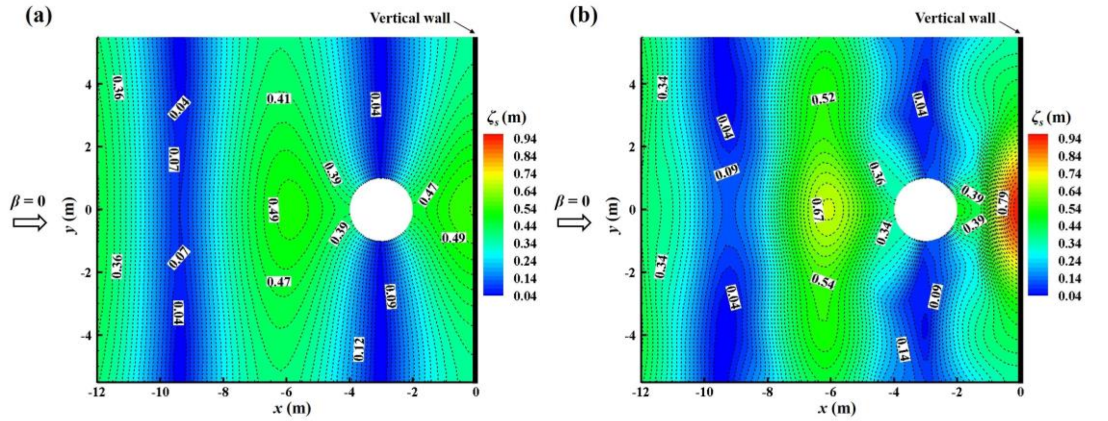

Fig. 21 Distribution of ζ_s around a cylinder situated near a wall at ka = 0.48 with a = 1 m, R = 3a, d = 3a, β = 0, and kA = 0.1 to the (a) first-order accuracy and (b) second-order accuracy

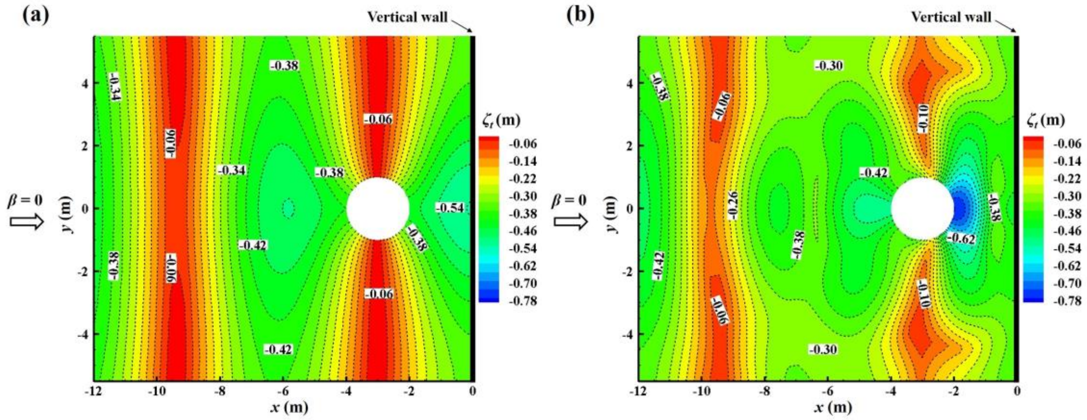

Fig. 22 Distribution of ζ_t around a cylinder situated near a wall at ka = 0.48 with a = 1 m, R = 3a, d = 3a, β = 0, and kA = 0.1 to the (a) first-order accuracy and (b) second-order accuracy

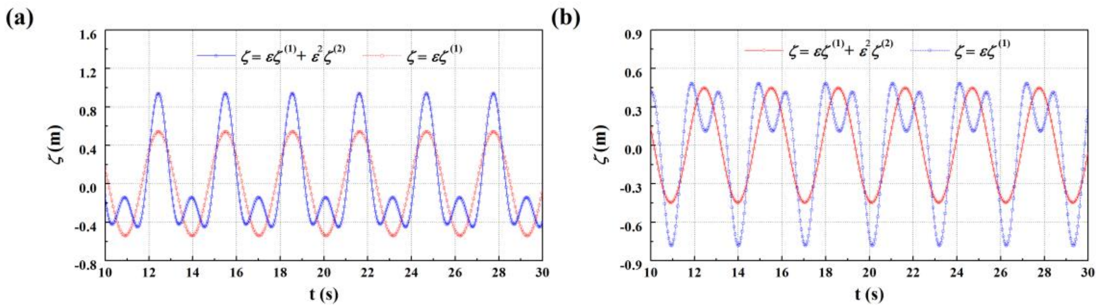

Fig. 23 Time history of the overall wave elevation at specific locations on a cylinder at ka = 0.48 with a = 1 m, R = 3a, d = 3a, β = 0, and kA = 0.1 at (a) (0, 0) and (b) (−2a, 0)

The distributions of ζ_s and ζ_t in the vicinity of a cylinder situated near a vertical wall are presented in Figs. 24 and 25 for $\beta = \pi/4$ with R = 3a. A change in the wave heading can clearly affect the wave elevation distribution as well as the locations where the maximum and minimum wave elevations appear. Fig. 26 shows the time history of the overall wave elevations at (0, 0.4a) and (−2.022a, −0.208a), respectively. At the former location, the maximum wave elevation is 0.503 m if the linear wave theory is adopted. If the second-order wave theory is adopted, it increases to 0.722 m. At the latter location, the minimum wave elevation can reach −0.639 m and −0.441 m, respectively, with and without the second-order effect. Above observations suggest that under oblique wave incidence, the corrections to the linear wave elevation due to the second-order effect are still obvious.

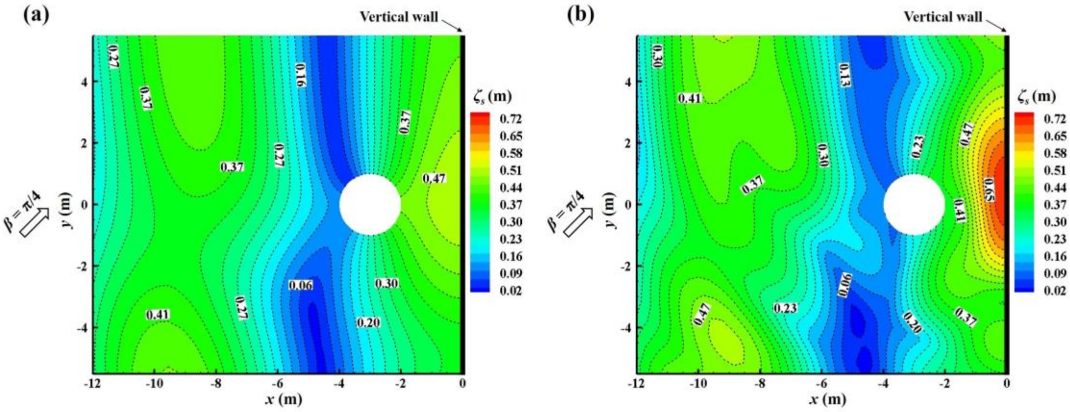

Fig. 24 Distribution of ζ_s around a cylinder situated near a wall at ka = 0.48 with a = 1 m, R = 3a, d = 3a, β = π/4, and kA = 0.1 to the (a) first-order accuracy and (b) second-order accuracy

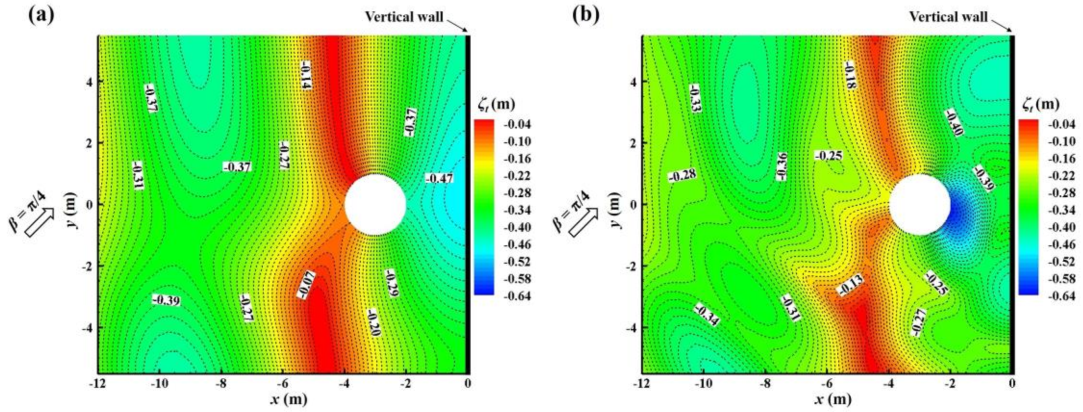

Fig. 25 Distribution of ζ_t around a cylinder situated near a wall at ka = 0.48 with a = 1 m, R = 3a, d = 3a, β = π/4, and kA = 0.1 to the (a) first-order accuracy and (b) second-order accuracy

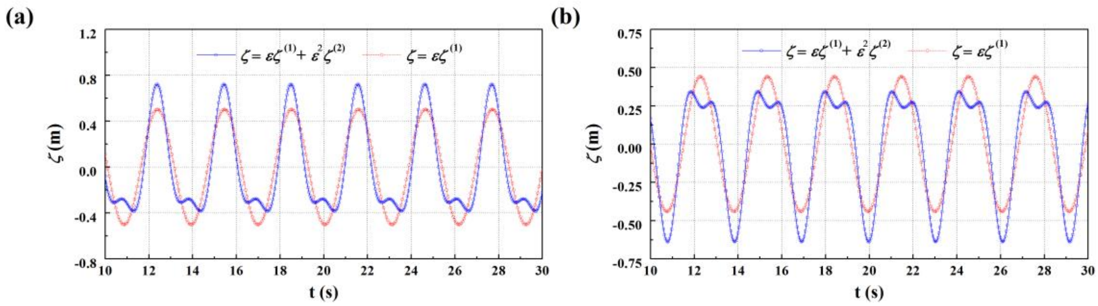

Fig. 26 Time history of the overall wave elevation at specific locations at ka = 0.48 with a = 1 m, R = 3a, d = 3a, β = π/4, and kA = 0.1 at (a) (0, 0.4a) and (b) (−2.022a, −0.208a)

5. Conclusion

In this study, a numerical model was proposed to evaluate the second-order wave run-up on a cylinder in front of a vertical wall. Based on the developed model, a detailed numerical analysis was conducted, and the effect of the vertical wall on the wave run-up on the cylinder was examined. The main conclusions of this study are summarised as follows.

1) The validity of the present solution was examined through a comparison with published data. The comparison confirms a favourable consistency between the results based on different methods.

2) There is a remarkable difference between the phenomenon of wave diffraction caused by a cylinder situated in front of a vertical wall and that in open seas. The first-order and second-order wave run-up on a cylinder near a vertical wall behave in an oscillatory manner around that experienced by a cylinder in open seas. Such oscillations gradually become less frequent as the cylinder gets closer to the wall. The effect of the vertical wall on the double-frequency wave run-up is generally more significant than that on the linear wave run-up. Owing to the influence of the vertical wall, a greatly amplified second-order wave run-up on the cylinder can be observed in the low-frequency region.

3) With the presence of the vertical wall, the wave field is obviously disturbed, and a pronounced wave run-up can be observed on the cylinder and on the vertical wall. The second-order effect can significantly enhance the wave elevation. Under normal wave incidence ($\beta = 0$), at the lee side of the cylinder and the centre of the vertical wall, the wave run-up based on the second-order wave theory can greatly exceed that based on the linear wave theory. Even when the wave steepness is small, the second-order wave elevation component can still make an apparent correction to the wave elevation distribution in the vicinity of the cylinder near the vertical wall.

The pronounced wave run-up should be accompanied by a large force on the structure. In addition to the wave run-up, an evaluation of the wave force is also a key element in the design of offshore structures, and an investigation of the wave force on structures situated near a wharf or breakwater is also of significant importance. This provides an interesting research topic for our future work.

Acknowledgement

The work is supported by the National Natural Science Foundation of China (Grant Nos. 51809037 and 51879039).

Reference

[1] Andersen T L, Frigaard P, Damsgaard M L, De Vos L. Wave run-up on slender piles in design conditions - Model tests and design rules for offshore wind. Coastal Engineering, 2011, 58(4): 281-289.

[2] Bai W, Eatock Taylor R. Numerical simulation of fully nonlinear regular and focused wave diffraction around a vertical cylinder using domain decomposition. Applied Ocean Research, 2007, 29(1): 55-71.

[3] Bai W, Feng X Y, Eatock Taylor R, Ang K K. Fully nonlinear analysis of near-trapping phenomenon around an array of cylinders. Applied Ocean Research, 2014, 44: 71-81.

[4] Bai W, Teng B. Simulation of second-order wave interaction with fixed and floating structures in time domain. Ocean Engineering, 2013, 74: 168-177.

[5] Bonakdar L, Oumeraci H, Etemad-Shahidi A. Run-up on vertical piles due to regular waves: Small-scale model tests and prediction formulae. Coastal Engineering, 2016, 118: 1-11.

[6] Cao D P, Huang Z H, He F, Wei J, Lo E Y -M. An improved prediction for wave run-up on a circular cylinder. Coastal Engineering Journal, 2017, 59(3): 13.

[7] Chatjigeorgiou I K. Semi-analytical solution for the water wave diffraction by arrays of truncated circular cylinders in front of a vertical wall. Applied Ocean Research, 2019, 88: 147-159.

[8] Chen X B. Middle-field formulation for the computation of wave-drift loads. Journal of Engineering Mathematics, 2007, 59(1): 61-82.

[9] Cong P W, Gou Y, Teng B. A new approach to low-frequency QTF and its application in predicting slow drift force. Ocean Engineering, 2012, 53: 25-37.

[10] Cong P W, Gou Y, Teng B, Zhang K, Huang Y F. Model experiments on wave elevation around a four-cylinder structure. Ocean Engineering, 2015, 96: 40-55.

[11] Cong P W, Bai W, Teng B, Gou Y. Semi-analytical solution to the second-order wave loads on a vertical cylinder in bi-chromatic bi-directional waves. Ocean Engineering, 2018, 161: 205-220.

[12] Cong P W, Bai W, Teng B. Analytical modeling of water wave interaction with a bottom-mounted surface-piercing porous cylinder in front of a vertical wall. Journal of Fluids and Structures, 2019, 88: 292-314.

[13] Cong P W, Chen L F, Gou Y. Hydrodynamic interaction among multiple columns in front of a vertical wall. Ocean Engineering, 2020, 197: 106877.

[14] De Vos L, Frigaard P, De Rouck J. Wave run-up on cylindrical and cone shaped foundations for offshore wind turbines. Coastal Engineering, 2007, 54(1): 17-29.

[15] Eatock Taylor R, Chau F P. Wave diffraction theory—some developments in linear and nonlinear theory. Journal of Offshore Mechanics and Arctic Engineering, 1992, 114(3): 185-194.

[16] Hallermeier R J. Nonlinear flow of wave crests past a thin pile. Journal of the Waterways Harbors and Coastal Engineering Division, 1976, 102(4): 365-377.

[17] Havelock T H. The pressure of water waves on a fixed obstacle. Proceedings of Royal Society, London, Series A. 1940, 175: 409-421.

[18] Isaacson M, Cheung K F. Time domain second-order wave diffraction in three dimensions. Journal of Waterway, Port, Coastal and Ocean Engineering, 1992, 118: 496-516.

[19] Kazeminezhad M H, Etemad-Shahidi A. A new method for the prediction of wave run-up on vertical piles. Coastal Engineering, 2015, 98: 55-64.

[20] Kim M H. Second-harmonic vertical wave loads on arrays of deep-draft circular cylinders in monochromatic uni- and multi-directional waves. Applied Ocean Research, 1993, 15(5): 245-262.

[21] Kim M H, Yue D K P. The complete second-order diffraction solution for an axisymmetric body. Part 1. Monochromatic incident waves. Journal of Fluid Mechanics, 1989, 200: 235-264.

[22] Kim Y W, Kring D C, Sclavounos P D. Linear and nonlinear interactions of surface waves with bodies by a three-dimensional Rankine panel method. Applied Ocean Research, 1997, 19(5-6): 235-249.

[23] Kriebel D L. Nonlinear wave interaction with a vertical circular cylinder. Part I: Diffraction theory. Ocean Engineering, 1990, 17(4): 345-377.

[24] Kriebel D L. Nonlinear wave interaction with a vertical circular cylinder. Part II: Wave run-up. Ocean Engineering, 1992, 19(1): 75-99.

[25] Lighthill J. Waves and hydrodynamic loading. Proceedings of the 2nd International Conference on the Behaviour of Offshore Structures, London, UK, 1979: 363-370.

[26] Malenica Š, Eatock Taylor R, Huang J B. Second-order water wave diffraction by an array of vertical cylinders. Journal of Fluid Mechanics, 1999, 390: 349-373.

[27] Mavrakos S A, Chatjigeorgiou I K. Second-order diffraction by a bottom-seated compound cylinder. Journal of fluids and structures, 2006, 22(4): 463-492.

[28] McCamy R. C, Fuchs R A. Wave forces on piles: Diffraction theory. Tech. Rep. 69. Beach Erosion Board, U.S. Army Corps of Engineers, 1954.

[29] Mei C C, Stiassnie M, Yue D K -P. Theory and applications of ocean surface waves. 2005, World Scientific, Singapore.

[30] Molin B. Second-order diffraction loads upon three-dimensional bodies. Applied Ocean Research, 1979, 1(4): 197-202.

[31] Niedzwecki J M, Duggal A S. Wave run-up and forces on cylinders in regular and random waves. Journal of Waterway, Port, Coastal and Ocean Engineering, 1992, 118(60: 615-634.

[32] Niedzwecki J M, Huston J R. Wave run-up and forces on cylinders in regular and random waves. Ocean Engineering, 1992, 19(1): 21-37.

[33] Ning D Z, Teng B, Song X Q. Analytical study on wave diffraction from a vertical circular cylinder in front of orthogonal vertical walls. Marine Science Bulletin. 2005, 7(1), 1-9.

[34] Ogilvie T F. Second-Order Hydrodynamic Effects on Ocean Platforms. Proceedings of the International Workshop Ship and Platform Motion, Berkeley, California, USA, 1983, 205-265.

[35] Shao Y L, Faltinsen O M. Second-order diffraction and radiation of a floating body with small forward speed. Journal of Offshore Mechanics and Arctic Engineering, 2013, 135(1): 011301.

[36] Sun L, Eatock Taylor R, Taylor P H. First- and second-order analysis of resonant waves between adjacent barges. Journal of Fluids and Structures, 2010, 26(6): 954-978.

[37] Sun L, Zong Z, Dong G H. Action of ship waves on a vertical cylinder in front of a vertical wall. In: Zhuang F G, Li J C. (eds) New Trends in Fluid Mechanics Research. 2007, Springer, Berlin, Heidelberg.

[38] Teng B, Eatock Taylor R. New higher-order boundary element methods for wave diffraction/radiation. Applied Ocean Research, 1995, 17(2): 71-77.

[39] Teng B, Ning D Z, Zhang X T. Wave radiation by a uniform cylinder in front of a vertical wall. Ocean engineering, 2004, 31(2): 201-224.

[40] Vazquez J H. Hydrodynamics loads on offshore structures in bichromatic bidirectional seas. University of Houston, 1995.

[41] Wang C Z, Wu G X. Interactions between fully nonlinear water waves and cylinder arrays in a wave tank. Ocean Engineering, 2010, 37(4): 400-417.

[42] Zheng S M, Zhang Y L. Teng B. Wave diffraction from a truncated cylinder in front of a vertical wall. Ocean Engineering, 2015, 104: 329-343.

[43] Zhou B Z, Teng B, Ning D Z, Cong P W. Fully nonlinear wave diffraction by a velocity potential division method. In Proceedings of the Twenty-second International Offshore and Polar Engineering Conference. International Society of Offshore and Polar Engineers, Rhodes, Greece, June 17-22, 2012.